Choice of computational method for swimming and pumping with nonslender helical filaments at low Reynolds number

Cite as: Phys. Fluids **28**, 021901 (2016); https://doi.org/10.1063/1.4940904
Submitted: 16 June 2015 . Accepted: 05 January 2016 . Published Online: 02 February 2016

J. D. Martindale, M. Jabbarzadeh, and H. C. Fu

PHYSICS OF FLUIDS **28**, 021901 (2016)

Choice of computational method for swimming and pumping with nonslender helical filaments at low Reynolds number

J. D. Martindale, M. Jabbarzadeh, and H. C. Fu
Department of Mechanical Engineering, University of Nevada, Reno, Nevada 89557, USA

(Received 16 June 2015; accepted 5 January 2016; published online 2 February 2016)

The flows induced by biological and artificial helical filaments are important to many possible applications including microscale swimming and pumping. Microscale helices can span a wide range of geometries, from thin bacterial flagella to thick helical bacterial cell bodies. While the proper choice of numerical method is critical for obtaining accurate results, there is little guidance about which method is optimal for a specified filament geometry. Here, using two physical scenarios — a swimmer with a head and a pump — we establish guidelines for the choice of numerical method based on helical radius, pitch, and filament thickness. For a range of helical geometries that encompass most natural and artificial helices, we create benchmark results using a surface distribution of regularized Stokeslets and then evaluate the accuracy of resistive force theory, slender body theory, and a centerline distribution of regularized Stokeslets. For the centerline distribution of regularized Stokeslets or slender body theory, we tabulate appropriate blob size and Stokeslet spacing or segment length, respectively, for each geometry studied. Finally, taking the computational cost of each method into account, we present the optimal choice of numerical method for each filament geometry as a guideline for future investigations involving filament-induced flows. © *2016 AIP Publishing LLC.* [http://dx.doi.org/10.1063/1.4940904]

I. INTRODUCTION

Low Reynolds number flows induced by filaments are commonly encountered in microscale scenarios. They occur in the swimming of microorganisms such as bacteria and spermatozoa,[1] as well as artificial flagella.[2–6] Furthermore, cilia- and flagella-induced microscale pumping is used in applications such as particle transport in biological systems[7,8] and the regulation and transport of fluids by fabricated systems utilizing bacterial flagella.[9] Filament-induced flows have been modeled using Resistive Force Theory (RFT), slender body theory (SBT), and boundary element methods (BEMs). For the slender filaments encountered in flagellar (bacterial and eukaryotic) swimming, there is some guidance in the literature as to which of these methods to use. Resistive force theory has been found to be inaccurate relative to slender body theory results,[10] while slender body theory and boundary element methods have compared favorably.[11,12] Recently, it has been shown that for slender helical filaments, RFT also gives misleading results in comparison to experiments.[13] However, not all helical filaments of interest are as slender as flagella, and there is less guidance available for the choice of method for thicker filaments. Thicker helical filaments can be realized in the helical cell bodies of many motile bacteria and are also important for magnetically actuated microscale swimming used for microrobotics, which could be used in medical applications such as *in vivo* surgery.[2,3,6,14,15]

While accurate and efficient computational models are needed for these filament-induced flows, it has not been established that which methods are appropriate for a given geometry given the wide range of filament thicknesses and helical pitches encountered, making it difficult for practitioners to make an informed choice without extensive numerical studies. Here, we compare the popular RFT, SBT, and two other methods based on the use of regularized Stokeslets. Each has different advantages and disadvantages in terms of ease of use, accuracy, and computational cost. Our objective

is to evaluate the accuracy and computational requirements of these methods across the range of geometries encountered in microscale applications in order to provide a guideline which may be used to make an informed choice of which numerical method to use for a given filament geometry.

What helical geometries are observed in the study of biological and artificial pumping and swimming applications? Consider a rigid helical filament whose geometry depends on three dimensionless parameters (see Fig. 1(a)): the ratio of the filament radius to helical radius $\tilde{a} = a/R$, the ratio of helical pitch to helical radius $\tilde{p} = p/R$, and the number of turns. In this study, we vary the parameters $\tilde{a}$ and $\tilde{p}$ to encompass the range of geometries encountered across most applications. Because Rodenborn *et al.*[13] find that the accuracy of SBT and the method of regularized Stokeslets are not dependent on total arclength, in this study we keep the arclength fixed at 3 pitch lengths.

Bacterial flagella are the thinnest filaments in our study with a radius of $a = 0.012$ μm.[16] For bacteria such as *Salmonella* and *E. coli*, the flagella may undergo polymorphic transformations between helical forms categorized by the number (n) of "R"-type protofilaments in the flagellum.[16–18] These polymorphic forms have a wide variation in both $\tilde{a}$ and $\tilde{p}$. For example, the normal ($n = 2$) form has values of $\tilde{a} = 0.023$ and $\tilde{p} = 1.611$, while the curly I ($n = 5$) form, seen in flagellar unbundling, has values of $\tilde{a} = 0.029$ and $\tilde{p} = 8.724$.[18] In Fig. 1(b), we have noted $\tilde{a}$ and $\tilde{p}$ for the $n = 1, 2$, and 9 polymorphic forms. These different bacterial flagellar forms are important not only for swimming and chemotaxis but also in micropumping applications. While we do not take into account the fluid structure interactions in this study, our results are relevant to any approach which would add deformations to the hydrodynamic interactions, such as for understanding the hydrodynamics associated with transformations between polymorphic configurations of these bacterial flagella.

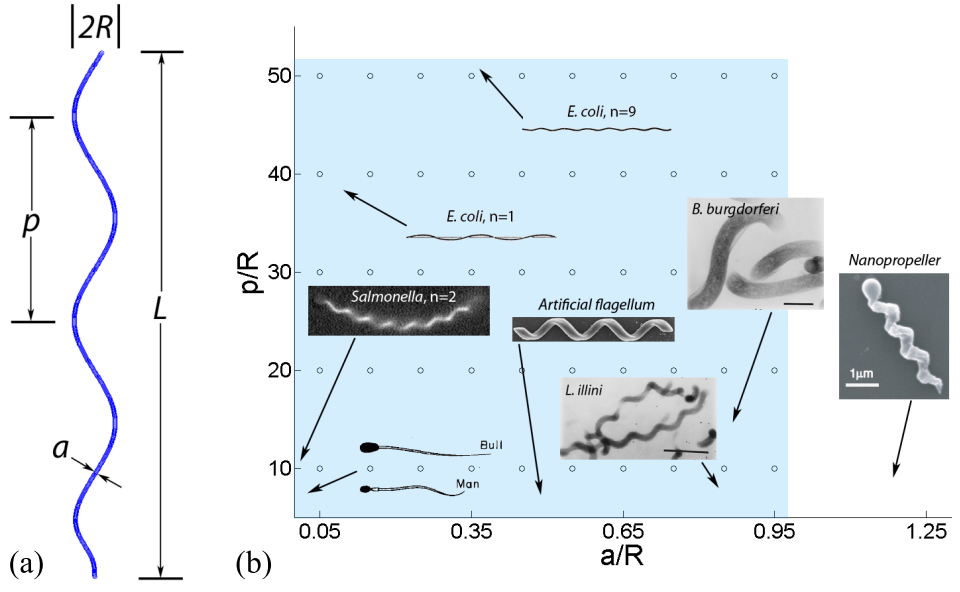

FIG. 1. (a) Geometry for helical filament in terms of filament radius a, helical pitch p, helical radius R, and helical length L. (b) Range of $\tilde{a} = a/R$ and $\tilde{p} = p/R$ values spanned by natural and artificial examples.[3,4,16,19,28] The shaded region indicates the geometry range investigated in this study; circles represent the specific investigated geometries. [*Nanopropeller* reprinted with permission from Ghosh *et al.*, "Dynamical configurations and bistability of helical nanostructures under external torque," Phys. Rev. E **86**, 031401 (2012). Copyright 2012 American Physical Society. *Artificial flagellum* reprinted with permission from C. Peters, O. Ergeneman, B. J. Nelson, and C. Hierold, in *2013 IEEE 26th International Conference on Micro Electro Mechanical Systems (MEMS)* (IEEE, 2013), pp. 564-567. Copyright 2013 IEEE. *Salmonella, n = 2* reprinted with permission from N. Darnton and H. C. Berg, "Force-extension measurements on bacterial flagella: Triggering polymorphic transformations," Biophys. J. **92**, 2230-2236 (2007). Copyright 2007 Elsevier. *Bull, Man spermatozoa* reprinted with permission from C. Brennen and H. Winet, "Fluid mechanics of propulsion by cilia and flagella," Annu. Rev. Fluid Mech. **9**, 339–398 (1977). Copyright 1977 Annual Reviews Inc. *L. illini and B. burgdorferi* reprinted with permission from S. Goldstein, K. Buttle, and N. Charon, "Structural analysis of the Leptospiraceae and Borrelia burgdorferi by high-voltage electron microscopy," J. Bacteriol **178**, 6539–6545 (1996). Copyright 1996 American Society for Microbiology.]

At the slender end of the spectrum, we also find the flagella of various mammalian spermatozoa, whose waveforms were presented by Brennen and Winet.[19] Human spermatozoa have a filament radius of $a \approx 0.25$ μm, around 20 times larger than that of bacterial flagella. However, due to their larger helical radius, their values of $\tilde{a}$ and $\tilde{p}$ are on the same order as those of bacterial flagella, with $\tilde{a}$ ranging from 0.01 for bull spermatozoa to 0.05 for human spermatozoa, and $\tilde{p} \approx 10$.[19]

For the slender regime of bacterial and eukaryotic flagella, Brennen and Winet note that the slender body theory originally proposed by Lighthill[20] or the resistive force theory of Gray and Hancock[21] should be applicable. Although there are many well-known variants of slender body theory,[22–26] in this study, as a representative SBT, we use the implementation proposed by Higdon,[27] which is equivalent to Lighthill's and which provides a relatively easy to implement numerical framework.

Rodenborn *et al*. focus on the slender regime up to $\tilde{a} = 0.0625$, but thicker helical filaments are common. For example, spirochetes have helical or wavy cell bodies, such as *L. illini*, with $\tilde{a} = 0.835$ and $\tilde{p} = 7.977$, and *B. burgdorferi*, with $\tilde{a} = 0.868$ and $\tilde{p} = 14.895$.[28] Along with these spirochetes, thick filaments include artificial swimmers such as the magnetically actuated nanopropellers fabricated and studied by Ghosh *et al*.[2,3,29] with $\tilde{a} = 1.188$ and $\tilde{p} = 5.688$, and the artificial flagella studied by Peters and others[4,5] with $\tilde{a} = 0.483$ and $\tilde{p} = 5.517$. In this regime, we would expect the previously mentioned theories to fail as the filament is no longer slender.[27] Instead, to obtain accurate results, typically one must employ a BEM.[30] As a simple implementation of a BEM, we utilize the method of regularized Stokeslets, which covers the surface of an object with continuous analogues of the classical Stokes flow singularities[14,31–34] and has gained popularity due to its ease of use. Recent work on swimming sperm[35] and the beating patterns of cilia[8] have also distributed regularized Stokeslets along filament centerlines rather than at the surface, which yields significant savings in computational effort, so we also examine such centerline distributions of regularized Stokeslets. Optimal parameters have been found for centerline distributions for slender ellipsoids,[36] which may be used to model straight rods, but not for helical filaments.

To summarize the range of biological and artificial helical filaments encountered in microscale applications, in Fig. 1(b), we plot a number of the examples mentioned above in $\tilde{a}$ and $\tilde{p}$ space. In the following investigation, we will examine geometries with $\tilde{a}$ between 0.05 and 0.95 in increments of 0.1, and $\tilde{p}$ between 10 and 50 in increments of 10, which encompass most of the physical and artificial microswimmers seen in Fig. 1(b).

Our investigation evaluates the accuracy of resistive force theory, the centerline distribution of regularized Stokeslets, and the slender body theory for two physical scenarios by comparing to benchmark results obtained from surface distributions of regularized Stokeslets, which are verified by convergence studies. The first scenario we consider is that of a swimmer with an ellipsoidal head and helical flagellum (seen in Fig. 2). The swimmer is force-free ($\mathbf{F} = \mathbf{0}$) and is driven by setting a constant relative angular velocity $\boldsymbol{\omega}$ between the body and flagellum. The outputs we use to evaluate accuracy in this scenario are the translational velocity $\mathbf{V}$ and the total torque $\mathbf{N_f}$ on the flagellum. The second scenario we consider is a pump created by a rotating helical filament attached to a no-slip plane (seen in Fig. 2). Since the filament is fixed to a plane, the translational velocity is $\mathbf{V} = \mathbf{0}$, and to drive the pump, we apply a constant torque $\mathbf{N}$ to the filament. The outputs used

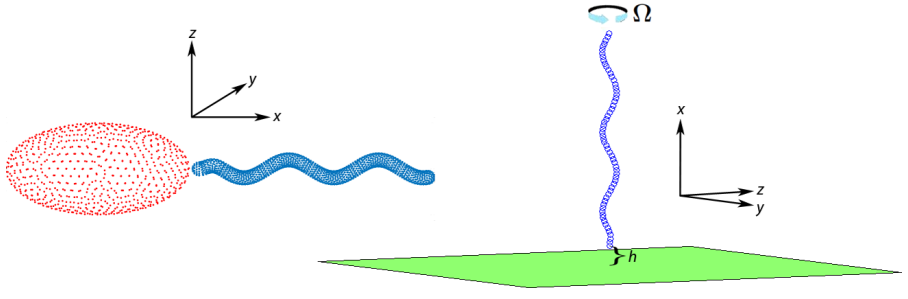

FIG. 2. The two physical scenarios modeled in this study: swimmer (left), pump (right).

to evaluate accuracy are the total force on the filament $\mathbf{F}$ and the angular velocity $\mathbf{\Omega}$. These two scenarios differ enough that they may be used as representatives for a broad range of applications.

Finally, we combine evaluation of the accuracy of resistive force theory, slender body theory, and the centerline distribution of regularized Stokeslets with an analysis of the relative computational cost for each method. The end result is a framework that can guide the choice of an optimal numerical method for a given filament geometry, which we hope will be broadly useful to researchers encountering flows caused by helical filaments in microscale applications.

II. NUMERICAL METHODS

In practice, SBT and methods involving regularized Stokeslets involve a similar procedure: the flow is created by an unknown force distribution, either on a surface for the method of regularized Stokeslets or on the filament centerline for slender body theory and centerline regularized Stokeslets. No-slip boundary conditions are imposed by setting the flow velocities at a set of collocation points equal to the velocity specified from the kinematics of the object. The result is the formation of a linear system of equations which may be solved to find the force distribution and hence velocity field everywhere. In equations, if $\mathbf{r}^0$ is the origin of the body frame, $\mathbf{V}$ is the translational velocity, and $\mathbf{\Omega}$ is the angular velocity about $\mathbf{r}^0$, then the velocity at point α is given by

$$\mathbf{u}(\mathbf{r}^\alpha) \equiv \mathbf{u}^\alpha = \mathbf{V} + \mathbf{\Omega} \times \Delta\mathbf{r}^\alpha, \tag{1}$$

where $\Delta\mathbf{r}^\alpha = \mathbf{r}^\alpha - \mathbf{r}^0$. Since this is a linear equation, we may write it in terms of the 3×6 matrix $\mathbf{k}^\alpha$,

$$\mathbf{u}^\alpha = \mathbf{k}^\alpha \begin{pmatrix} \mathbf{V} \\ \mathbf{\Omega} \end{pmatrix} = \begin{pmatrix} 1 & 0 & 0 & 0 & \Delta r_z^\alpha & -\Delta r_y^\alpha \\ 0 & 1 & 0 & -\Delta r_z^\alpha & 0 & \Delta r_x^\alpha \\ 0 & 0 & 1 & \Delta r_y^\alpha & -\Delta r_x^\alpha & 0 \end{pmatrix} \begin{pmatrix} \mathbf{V} \\ \mathbf{\Omega} \end{pmatrix}. \tag{2}$$

This allows us to represent the velocity at the collocation points of the system as

$$\mathbf{U} \equiv \begin{pmatrix} \mathbf{u}^1 \\ \vdots \\ \mathbf{u}^N \end{pmatrix} = \begin{pmatrix} \mathbf{k}^1 \\ \vdots \\ \mathbf{k}^N \end{pmatrix} \begin{pmatrix} \mathbf{V} \\ \mathbf{\Omega} \end{pmatrix} \equiv \mathbf{K} \begin{pmatrix} \mathbf{V} \\ \mathbf{\Omega} \end{pmatrix}, \tag{3}$$

where $\mathbf{K} \in \mathbb{R}^{3N \times 6}$. Note that we use a capital letter $\mathbf{U}$ to represent the $3\mathrm{N} \times 1$ vector containing the N velocities of all collocation points and similarly a capital $\mathbf{K}$ which is composed of all $N\,\mathbf{k}^\alpha$. To satisfy no-slip boundary conditions, the velocity specified by the kinematics is set equal to the fluid velocity at the collocation points. Thus, the fluid velocity vector $\mathbf{U}$ can also be written as

$$\mathbf{U} = \begin{pmatrix} \mathbf{g}^{1,1} & \mathbf{g}^{1,2} & \cdots & \mathbf{g}^{1,N} \\ \mathbf{g}^{2,1} & \mathbf{g}^{2,2} & \cdots & \mathbf{g}^{2,N} \\ \vdots & \vdots & \ddots & \vdots \\ \mathbf{g}^{N,1} & \mathbf{g}^{N,2} & \cdots & \mathbf{g}^{N,N} \end{pmatrix} \begin{pmatrix} \mathbf{p}^1 \\ \vdots \\ \mathbf{p}^\mathbf{N} \end{pmatrix} \equiv \mathbf{GP}, \tag{4}$$

where $\mathbf{G} \in \mathbb{R}^{3N \times 3N}$ and $\mathbf{P} \in \mathbb{R}^{3N \times 1}$ contains the 3×1 force $\mathbf{p}^\alpha$ at each collocation point. We call the submatrices $\mathbf{g}^{\alpha,\beta} \in \mathbb{R}^{3\times 3}$ the *kernel*. The kernel represents the velocity at point α due to a force at point β. Each numerical method in our study can be specified by choosing a different kernel.

A. BEM for flagellar filament above a no-slip plane

For the case of a rotating helical filament attached to a no-slip plane, we choose $\mathbf{r}^0 = \mathbf{0}$ at the attachment point at the plane surface (see Fig. 2) and represent the total force and torque on the body as

$$\mathbf{F} = \sum_{\alpha=1}^{N} \mathbf{p}^\alpha, \tag{5}$$

$$\mathbf{N} = \sum_{\alpha=1}^{N} \Delta\mathbf{r}^{\alpha} \times \mathbf{p}^{\alpha}, \tag{6}$$

which can be written as

$$\begin{pmatrix} \mathbf{F} \\ \mathbf{N} \end{pmatrix} = \mathbf{K}^T \mathbf{P}. \tag{7}$$

Enforcing the no-slip boundary condition on the surface of the filament lets us to form a relationship between the velocities $\mathbf{V}$ and $\boldsymbol{\Omega}$, and the total force $\mathbf{F}$ and torque $\mathbf{N}$ on the filament. Solving Eq. (4) for $\mathbf{P} = \mathbf{G}^{-1}\mathbf{U}$ and using Eqs. (3) and (7),

$$\begin{pmatrix} \mathbf{F} \\ \mathbf{N} \end{pmatrix} = \mathbf{K}^T \mathbf{G}^{-1} \mathbf{K} \begin{pmatrix} \mathbf{V} \\ \boldsymbol{\Omega} \end{pmatrix} = \mathbf{R} \begin{pmatrix} \mathbf{V} \\ \boldsymbol{\Omega} \end{pmatrix} = \begin{pmatrix} \mathbf{R_T} & \mathbf{R_C} \\ \mathbf{R_C}^T & \mathbf{R_R} \end{pmatrix} \begin{pmatrix} \mathbf{V} \\ \boldsymbol{\Omega} \end{pmatrix}, \tag{8}$$

where $\mathbf{R} = \mathbf{K}^T\mathbf{G}^{-1}\mathbf{K}$ is the resistance matrix with 3×3 translational, rotational, and coupling components denoted by $\mathbf{R_T}$, $\mathbf{R_R}$, and $\mathbf{R_C}$, respectively. We apply a constant torque $\mathbf{N}$ tangential to the axis of the filament and set the translational velocity $\mathbf{V} = \mathbf{0}$ since the filament remains anchored above the $x = 0$ plane. These constraints yield the system

$$\begin{pmatrix} \mathbf{F} \\ \mathbf{N} \end{pmatrix} = \begin{pmatrix} \mathbf{R_C} \\ \mathbf{R_R} \end{pmatrix} \boldsymbol{\Omega}, \tag{9}$$

with solution

$$\boldsymbol{\Omega} = \mathbf{R_R}^{-1}\mathbf{N}, \tag{10}$$

$$\mathbf{F} = \mathbf{R_C}\mathbf{R_R}^{-1}\mathbf{N}. \tag{11}$$

B. BEM for swimmer with ellipsoidal head

For the swimmer with an ellipsoidal head, we choose the origin of the body-fixed frame $\mathbf{r^0}$ as the flagellum attachment point on one end of the head (see Fig. 2). A surface distribution of regularized Stokeslets is always used to model the head, and these collocation points are denoted as $\mathbf{r_h^{\alpha_1}}$ for $1 \le \alpha_1 \le N_1$. The collocation points on the flagellum are denoted as $\mathbf{r_f^{\alpha_2}}$ for $1 \le \alpha_2 \le N_2$. In this scenario, $\mathbf{V}$ and $\boldsymbol{\Omega}$ represent the translation and rotation about the origin. Here, the kinematics specify

$$\mathbf{u_h}(\mathbf{r_h^{\alpha_1}}) = \mathbf{u_h^{\alpha_1}} = \mathbf{V} + \boldsymbol{\Omega} \times \Delta\mathbf{r_h^{\alpha_1}}, \tag{12}$$

$$\mathbf{u_f}(\mathbf{r_f^{\alpha_2}}) = \mathbf{u_f^{\alpha_2}} = \mathbf{V} + \boldsymbol{\Omega} \times \Delta\mathbf{r_f^{\alpha_2}} + \mathbf{k}_{\times}^{\alpha_2}\boldsymbol{\omega}, \tag{13}$$

where $\boldsymbol{\omega} = (\omega, 0, 0)^T$ is the specified relative rotation rate between the head and flagellum and

$$\mathbf{k}_{\times}^{\alpha_2} = \begin{pmatrix} 0 & \Delta r_z^{\alpha_2} & -\Delta r_y^{\alpha_2} \\ -\Delta r_z^{\alpha_2} & 0 & \Delta r_x^{\alpha_2} \\ \Delta r_y^{\alpha_2} & -\Delta r_x^{\alpha_2} & 0 \end{pmatrix}.$$

As in Section II, this is a linear system of equations and can be written as

$$\begin{pmatrix} \mathbf{U_h} \\ \mathbf{U_f} \end{pmatrix} \equiv \begin{pmatrix} \mathbf{u_h^1} \\ \vdots \\ \mathbf{u_h^{N_1}} \\ \mathbf{u_f^1} \\ \vdots \\ \mathbf{u_f^{N_2}} \end{pmatrix} = \begin{pmatrix} \mathbf{k}^{\alpha_1=1} \\ \vdots \\ \mathbf{k}^{\alpha_1=N_1} \\ \mathbf{k}^{\alpha_2=1} \\ \vdots \\ \mathbf{k}^{\alpha_2=N_2} \end{pmatrix} \begin{pmatrix} \mathbf{V} \\ \boldsymbol{\Omega} \end{pmatrix} + \dot{\mathbf{L}} \equiv \mathbf{K} \begin{pmatrix} \mathbf{V} \\ \boldsymbol{\Omega} \end{pmatrix} + \dot{\mathbf{L}}, \tag{14}$$

where $\mathbf{K} \in \mathbb{R}^{3(N_1+N_2)\times 6}$, $\mathbf{U_h} \in \mathbb{R}^{3N_1\times 1}$ is the velocity at each collocation point on the head, $\mathbf{U_f} \in \mathbb{R}^{3N_2\times 1}$ is the velocity at each collocation point on the flagellum, and $\dot{\mathbf{L}} \in \mathbb{R}^{3(N_1+N_2)\times 1}$ is

$$\dot{\mathbf{L}} = \begin{pmatrix} \mathbf{0} \\ \vdots \\ \mathbf{0} \\ \mathbf{k}_{\times}^{\alpha_2=1} \\ \vdots \\ \mathbf{k}_{\times}^{\alpha_2=N_2} \end{pmatrix} \boldsymbol{\omega}.$$

On the other hand, the hydrodynamics specify

$$\begin{pmatrix} \mathbf{U_h} \\ \mathbf{U_f} \end{pmatrix} = \begin{pmatrix} \mathbf{G_{hh}} & \mathbf{G_{hf}} \\ \mathbf{G_{fh}} & \mathbf{G_{ff}} \end{pmatrix} \begin{pmatrix} \mathbf{P_h} \\ \mathbf{P_f} \end{pmatrix} = \mathbf{GP}, \tag{15}$$

where $\mathbf{G_{hh}} \in \mathbb{R}^{3N_1 \times 3N_1}$ and $\mathbf{G_{fh}} \in \mathbb{R}^{3N_2 \times 3N_1}$ give the velocity on the head and flagellum, respectively, due to the point forces $\mathbf{p}_{\mathbf{h}}^{\boldsymbol{\alpha_1}}$ located on the head, and $\mathbf{G_{hf}} \in \mathbb{R}^{3N_1 \times 3N_2}$ and $\mathbf{G_{ff}} \in \mathbb{R}^{3N_2 \times 3N_2}$ give the velocity on the head and flagellum, respectively, due to the point forces $\mathbf{p}_{\mathbf{f}}^{\boldsymbol{\alpha_2}}$ located on the flagellum. Enforcing no-slip boundary conditions requires that the kinematic and hydrodynamic velocities to be equal, which yields the equation

$$\mathbf{G} \begin{pmatrix} \mathbf{P_h} \\ \mathbf{P_f} \end{pmatrix} = \mathbf{K} \begin{pmatrix} \mathbf{V} \\ \boldsymbol{\Omega} \end{pmatrix} + \dot{\mathbf{L}}. \tag{16}$$

In this scenario, we also require that the net force and net torque be zero, so Eq. (7) implies

$$\mathbf{0} = \mathbf{K}^T \begin{pmatrix} \mathbf{P_h} \\ \mathbf{P_f} \end{pmatrix} = \mathbf{K}^T \mathbf{G}^{-1} \left(\mathbf{K} \begin{pmatrix} \mathbf{V} \\ \boldsymbol{\Omega} \end{pmatrix} + \dot{\mathbf{L}} \right). \tag{17}$$

This equation can be solved for $\mathbf{V}$ and $\boldsymbol{\Omega}$ to obtain

$$\begin{pmatrix} \mathbf{V} \\ \boldsymbol{\Omega} \end{pmatrix} = -\left(\mathbf{K}^T \mathbf{G}^{-1} \mathbf{K}\right)^{-1} \mathbf{K}^T \mathbf{G}^{-1} \dot{\mathbf{L}}, \tag{18}$$

where $\mathbf{M} = \left(\mathbf{K}^T \mathbf{G}^{-1} \mathbf{K}\right)^{-1}$ is the inverse of the resistance matrix, called the mobility matrix. In this scenario, the translational velocity $\mathbf{V}$ and the torque on the flagellum $\mathbf{N_f}$ are the outputs. To solve for the torque, we find $\mathbf{P_f}$ through Eq. (16) since $\mathbf{V}$ and $\boldsymbol{\Omega}$ are now known, giving

$$\mathbf{N_f} = \sum_{\alpha_2=1}^{N_2} \Delta \mathbf{r}^{\boldsymbol{\alpha_2}} \times \mathbf{p}_{\mathbf{f}}^{\boldsymbol{\alpha_2}}. \tag{19}$$

C. Resistive force theory for swimmer with ellipsoidal head

We also examine the accuracy of resistive force theory for the case of the swimmer. In resistive force theory, long-range hydrodynamic interactions are ignored, so we treat the hydrodynamics of the flagellum and head separately through their resistance matrices. The resistance matrix of the ellipsoidal head $\mathbf{R_h}$ may be calculated from analytical results, e.g., as presented in the textbook of Kim and Karrila.[37] Resistive force theory is used to calculate the resistance matrix of the helix as follows. The local force per unit length on the filament is

$$\mathbf{f}_{\mathrm{RFT}} = \xi_{\perp} \mathbf{v}_{\mathrm{rel}} + \left(\xi_{\parallel} - \xi_{\perp}\right) \hat{\mathbf{t}}\hat{\mathbf{t}} \cdot \mathbf{v}_{\mathrm{rel}}, \tag{20}$$

where $\mathbf{v}_{\mathrm{rel}} = \mathbf{V} + \boldsymbol{\Omega} \times \mathbf{r}$, $\hat{\mathbf{t}}$ is the local unit tangent vector, and the coefficients $\xi_{\parallel}$ and $\xi_{\perp}$ are drag coefficients obtained by slender body analysis. For the theories of Gray and Hancock[21] and Lighthill,[20] these coefficients are

$$\xi_{\parallel},\ \xi_{\perp} = \begin{cases} \dfrac{2\pi\mu}{\ln(2\tilde{p}/\tilde{a}) - 1/2},\ \dfrac{4\pi\mu}{\ln(2\tilde{p}/\tilde{a}) + 1/2} & \text{(Gray and Hancock)} \\ \dfrac{2\pi\mu}{\ln(0.18\tilde{p}/\tilde{a})},\ \dfrac{4\pi\mu}{\ln(0.18\tilde{p}/\tilde{a}) + 1/2} & \text{(Lighthill)} \end{cases}.$$

Note that in Lighthill's formula, we use the pitch as suggested by analysis of helical filaments.[38] The Lighthill coefficients might be expected to be more applicable since in a comparison of RFT and SBT for planar thin filaments, Johnson and Brokaw[10] found that the Lighthill coefficients adequately predicted local forces and torques on the filament, while the Gray and Hancock coefficients required ~35% adjustments to produce comparable accuracy. Integrating the force and torque $\mathbf{r} \times \mathbf{f}_{RFT}$ along the filament for various translational and rotational velocities yields the resistance matrix $\mathbf{R_f}$ of the flagellum. The origin of rotation for both $\mathbf{R_h}$ and $\mathbf{R_f}$ is the flagellum attachment point.

Given the resistance matrices, we require that the total force and torque be zero,

$$\mathbf{0} = \begin{pmatrix} \mathbf{F}_{\text{tot}} \\ \mathbf{N}_{\text{tot}} \end{pmatrix} = \begin{pmatrix} \mathbf{F_h} \\ \mathbf{N_h} \end{pmatrix} + \begin{pmatrix} \mathbf{F_f} \\ \mathbf{N_f} \end{pmatrix}, \tag{21}$$

and using Eq. (8), we may express the above equation as

$$\mathbf{0} = \mathbf{R_h} \begin{pmatrix} \mathbf{V} \\ \boldsymbol{\Omega} \end{pmatrix} + \mathbf{R_f} \begin{pmatrix} \mathbf{V} \\ \boldsymbol{\Omega} + \boldsymbol{\omega} \end{pmatrix}. \tag{22}$$

This equation is solved for $\mathbf{V}$ and $\boldsymbol{\Omega}$ to give

$$\begin{pmatrix} \mathbf{V} \\ \boldsymbol{\Omega} \end{pmatrix} = -(\mathbf{R_h} + \mathbf{R_f})^{-1} \mathbf{R_f} \begin{pmatrix} \mathbf{0} \\ \boldsymbol{\omega} \end{pmatrix}, \tag{23}$$

which gives us one of our outputs, the translational velocity $\mathbf{V}$. Using the relationship

$$\begin{pmatrix} \mathbf{F_f} \\ \mathbf{N_f} \end{pmatrix} = \mathbf{R_f} \begin{pmatrix} \mathbf{V} \\ \boldsymbol{\Omega} + \boldsymbol{\omega} \end{pmatrix}, \tag{24}$$

we find our second output, the torque on the flagellum $\mathbf{N_f}$.

D. Geometries

1. Filament

In each of the physical scenarios described in Section I, we consider a helical filament oriented in the positive x-direction of non-dimensional radius $\tilde{a}$ and non-dimensional helical pitch $\tilde{p}$ whose arclength is fixed at $\tilde{L} = L/R = 3\tilde{p}$. The filament centerline is described by

$$\mathbf{r_c}(s) = s\hat{\mathbf{x}} + \left(1 - e^{-s^2/k_E^2}\right) \left[\cos(2\pi s/\tilde{p})\hat{\mathbf{y}} + \sin(2\pi s/\tilde{p})\hat{\mathbf{z}}\right]. \tag{25}$$

The exponential term describes a tapering region near the attachment point, where $k_E = \tilde{p}/(2\pi)$ is the characteristic length of the tapering region.[14]

2. Helical swimmer

For the helical swimmer, we use an ellipsoidal cell body with semi-major and semi-minor axes which are $\tilde{a}_h = a_h/R = 10.204$ and $\tilde{b}_h = b_h/R = 5.102$, respectively. The major axis is placed along the x-axis, and a helical flagellum whose geometry is prescribed in Eq. (25) is attached at $x = 0$. The helix is translated away from the ellipsoid to create a gap between the head and flagellum in order to ensure accurate results for nearby moving surfaces.[14] An example of this geometry is seen in Fig. 2.

3. Filament above a no-slip plane

Here, we examine the rotation of a helical filament with its end at a distance of $\tilde{h} = 10\tilde{a}$ above a no-slip plane (Fig. 2). To model this scenario, we translate the centerline prescribed above by $\tilde{h}$ in the x-direction. This setup is inspired by pumping applications where pumping flows may be caused by the movement of filaments.

E. Numerical methods: Kernels and discretization

1. Method of regularized Stokeslets: Surface distribution

For the benchmark cases, we employ the method of regularized Stokeslets by distributing smoothed analogues of the classical Stokeslet on the filament surface or body.[31–33] In the following calculations, we make use of a standard smoothing function which depends on a "blob" parameter δ that describes the spread of the point forces and allows us to obtain non-singular numerical values for all calculations. A full description of the regularized Stokeslet is found in the literature,[31–33] and the kernel $\mathbf{g}^{\alpha,\beta}$ (defined in Section II) that we use for the method of regularized Stokeslets is given by Eq. (10*b*) in the work of Cortez *et al.*[33]

For discretization, the filament is divided into cross sections perpendicular to the centerline of the filament. We place n_c evenly spaced Stokeslets on the perimeter of each cross section, similar to the discretization described previously by Hyon *et al.*[14] The cross sections are spaced so that the distance between Stokeslets (Δs) on a given cross section is the same as the distance between successive cross sections. Therefore, $\Delta s = 2\tilde{a}\sin(\pi/n_c)$. This spacing means that the total number of Stokeslets increases rapidly as we increase the number of Stokeslets per cross section and as the filament radius decreases. For a given spacing, the blob parameter δ is set equal to the distance between Stokeslets, $\delta = \Delta s$.

For the discretization of the swimmer with an ellipsoidal head, each successive filament cross section is rotated by an angle π/n_c with respect to its normal axis in order to stagger the Stokeslets. Also, the ends of the filament are capped with hemispheres that are discretized using the grid method given by Cortez *et al.*[33] The ellipsoidal head is discretized by cutting into cross sections perpendicular to the major (fore-aft) axis. If we define Δs_h as the spacing between Stokeslets on the cell body and successive cross sections, the number of Stokeslets on each cross section depends on the radius of the cross section and is determined by $n_c = 2\pi r_h/\Delta s_h$, where $r_h = \tilde{b}_h\sqrt{1-(x/\tilde{a}_h)^2}$. Similarly to the flagellum, each successive cross section of the head is rotated by an angle $\Delta s_h/2r_h$ to stagger the Stokeslets on the cell body. For our investigation, $\Delta s_h = 0.1$ is the non-dimensional Stokeslet spacing on the head, and $N_1 = 750$ is the total number of regularized Stokeslets on the head.

The case of the filament rotating above a no-slip plane uses a slightly different discretization. The cross sections are not rotated about the normal axis of the filament, and there are no hemispherical caps added to the end of the filament. Most importantly, the kernel is modified to satisfy the no-slip boundary conditions at the planar boundary ($x = 0$). For the method of regularized Stokeslets, we employ a full regularized Blakeslet distribution which consists of the regularized Stokeslet and its corresponding image system mirrored about the $x = 0$ plane:[31] for a collocation point on the filament surface at $\mathbf{r}^\alpha = (h^\alpha, y^\alpha, z^\alpha)$, its image is located at a point $\mathbf{r}^\alpha_* = (-h^\alpha, y^\alpha, z^\alpha)$. In this scenario, the kernel $\mathbf{g}^{\alpha,\beta}$ is derived from Eq. (21) in the work of Ainley *et al.*[31]

2. Method of regularized Stokeslets: Centerline distribution

The flows around filaments have also been computed using a centerline distribution along the center of the filament instead of at the filament surface. For this method, we use the same kernels as in Section II E 1. For the swimmer, the head is always modelled using a surface distribution of regularized Stokeslets with spacing and blob size as defined in Sec. II E 1.

For both the swimmer and the pump, we discretize the filament centerline by placing regularized Stokeslets with blob size δ at equally spaced points along the filament centerline with spacing Δs. There is no *a priori* choice of Stokeslet spacing Δs or blob size δ, although physically the blob size is expected to be of the same order of magnitude as the filament radius. These parameters must be tuned for each geometry to obtain the most accurate result. We report the optimal parameter values for each geometry we study later; these provide starting points for studies determining the optimal parameter values for other geometries in future studies. Despite this, the positive aspects of this discretization are twofold. First, it still relies on the method of regularized Stokeslets, and so we may use the same kernels found in the works of Cortez *et al.*[33] and Ainley *et al.*,[31] which are relatively easy to implement. Second, the number of Stokeslets needed for the discretization is much lower than that of the surface distribution, increasing the computational efficiency of the method.

3. Slender body theory

In our investigation, we use the slender body theory outlined by Higdon[27] as a representative SBT. This method calculates the flow due to a distribution of classical Stokeslets and dipoles along the centerline of the filament. The force distribution $\mathbf{f}$ along the centerline is unknown, while the dipole strength $\mathbf{d} = -(\tilde{a}^2/4\mu)\mathbf{f}_\perp$ is specified to preserve no-slip boundary conditions on the surface of the filament. In Higdon's method, the filament centerline is discretized into small cylindrical segments of length $2q$, and the Stokeslet (and hence dipole strength) is assumed to be constant within each segment. The integral of the Stokeslet and dipole distribution along each segment can be evaluated analytically to yield the flow produced by each segment, which defines the kernel. The expression for the kernel we use can be found in Eq. (27) in the work of Higdon.[27] Similarly to the centerline distribution of regularized Stokeslets discussed in Sec. II E 2, the parameter q must be tuned to ensure the most accurate results, but the advantage is far fewer discretization elements than a surface discretization, especially for thin filaments.

For the swimmer, we always model the ellipsoidal head using the surface distribution of regularized Stokeslets described in Section II E 1. Therefore, the $\mathbf{G_{hh}}$ and $\mathbf{G_{fh}}$ submatrices in Eq. (16) are always formulated in terms of the regularized Stokeslet kernel discussed in Section II E 1. The other submatrices $\mathbf{G_{hf}}$ and $\mathbf{G_{ff}}$ are formulated using the kernel for the slender body theory.

For the case of a helical filament above a plane, we must include an image system to satisfy the no-slip condition on the plane. The singularities distributed along the centerline of the filament are Stokeslets *and* dipoles, and so the system is not simply a Blakeslet distribution since we must include the image system of the dipole.[25] To evaluate the contribution of the images, we integrate the contribution from each image segment numerically using Simpson's rule since they are non-singular at the collocation points on the filament centerline. The kernel for this method is defined by the sum of Eq. (27) in the work of Higdon[27] and the numerical integral of the Stokeslet and dipole image systems provided by Blake and Chwang.[25]

F. Error metric

In order to assess the accuracy of these methods, we examine an error metric which includes both output parameters, the swimming velocity $\mathbf{V}$ and torque on the filament $\mathbf{N_f}$ in the case of the swimmer, and the net force $\mathbf{F}$ and the angular velocity $\mathbf{\Omega}$ in the case of the pump,

$$E_{\text{swimmer}}\,(\%) = 100\sqrt{\left(\frac{|\mathbf{V}^b - \mathbf{V}|}{|\mathbf{V}^b|}\right)^2 + \left(\frac{|\mathbf{N_f}^b - \mathbf{N_f}|}{|\mathbf{N_f}^b|}\right)^2}, \tag{26}$$

$$E_{\text{pump}}\,(\%) = 100\sqrt{\left(\frac{|\mathbf{F}^b - \mathbf{F}|}{|\mathbf{F}^b|}\right)^2 + \left(\frac{|\mathbf{\Omega}^b - \mathbf{\Omega}|}{|\mathbf{\Omega}^b|}\right)^2}, \tag{27}$$

where we add the sum-squared error of each respective output. The "b" superscript denotes the output from the benchmark case using the surface distribution of regularized Stokeslets.

III. RESULTS

A. Convergence study for regularized Stokeslets on filament surface

In previous work,[14] we have shown that for geometries similar to those used here for swimming, the method of regularized Stokeslets agrees well with SBT and boundary element method results presented in the work of Phan-Thien *et al.*[11] For this study, we create benchmark results using the surface distribution of regularized Stokeslets and perform convergence studies for selected geometries for swimming and pumping. These sample cases correspond to $\tilde{p} = 20$ and $\tilde{a} = 0.05, 0.35, 0.65, 0.95$. For the swimmer, we examine the x-component of the non-dimensionalized translational velocity against the Stokeslet spacing Δs. For the pump, we examine the x-component of the non-dimensionalized force against Δs.

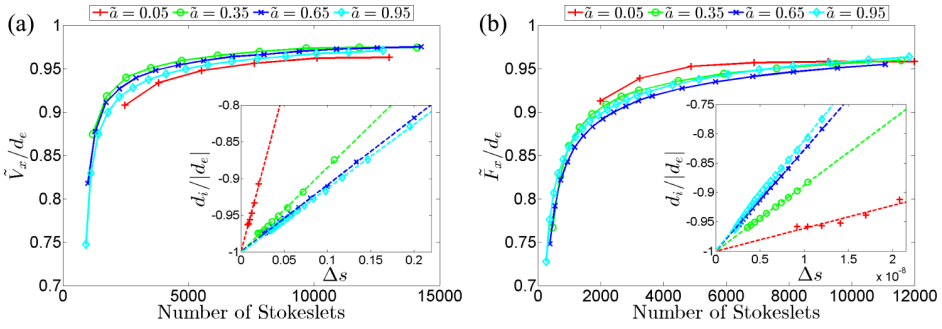

FIG. 3. Convergence studies for selected geometries of (a) swimmer (velocity normalized by extrapolant d_e) and (b) pump (force normalized by extrapolant d_e) using surface distribution of regularized Stokeslets. Inset in each figure is a plot of the data d_i normalized by the extrapolant against the Stokeslet spacing Δs with linear fit. As described in the text, the linear fit applies to each data set except for $\tilde{a} = 0.05$, for which it yields a conservative estimate of error. From these, we estimate that our results are converged to within 5% accuracy.

Fig. 3 presents the convergence studies for the swimmer and pump, respectively. In both cases, the quantity examined (either velocity or force) is normalized by a Richardson extrapolant obtained as described below, as a function of number of regularized Stokeslets used in the discretization. The extrapolant d_e for each case is obtained from the expectation that the error for each data point d_i obeys a power law relation to the discretization spacing Δs,

$$d_i - d_e = C\Delta s^{\gamma}, \tag{28}$$

where C and γ are constants. In each case, we examine the data for which γ is in the asymptotic range to obtain a fit for C and γ in the least-squared sense.

Ainley *et al*. find slightly greater than first order convergence when using a blob size $\delta \sim \Delta s^{0.9}$ for the problem of a sphere translating near a wall.[31] Since we use the similar $\delta = \Delta s$, we expect similar rates of convergence, and indeed in nearly all the cases, we find that $\gamma \approx 1$. To provide estimates of error, in the insets of Fig. 3, we show the fits to $d_i/|d_e|$ vs. Δs for $\gamma = 1$ over the asymptotic range. The swimming and pumping geometries with $\tilde{a} = 0.05$ (red crosses) display higher order behavior. In those cases, for consistency, we still find the extrapolant using $\gamma = 1$, which yields a conservative estimate of error. For the swimmer, the non-dimensionalized x-component of velocity for every geometry has converged to within 4% of the linear extrapolant. For the pump, the non-dimensionalized x-component of force has converged to within 5% of the linear extrapolant.

Based on these convergence studies, benchmark results for all the other geometries are generated using 8300 – 12 000 regularized Stokeslets for the swimmer and 10 000 – 12 500 regularized Stokeslets for the pump, for which we expect an error of less than 5%. These convergence studies also highlight the computational cost of this method and the motivation behind our investigation of other computationally cheaper numerical methods. The computational cost for all methods scales as N^3, where N is the total number of collocation points. As we will see in Secs. III B and III C, the method of regularized Stokeslets distributed on the filament centerline as well as the slender body theory provides a significant reduction in the total number of collocation points. This reduction comes at the cost of reduced accuracy, and so we examine the error due to each of these methods to assess their utility in various physical regimes.

B. Regularized Stokeslets distributed on the filament centerline

We now investigate the accuracy of the computationally cheaper methods outlined in Section II by comparing the results with the benchmarks obtained from calculations using the converged surface distribution of regularized Stokeslets. First, we present findings for the method of regularized Stokeslets distributed on the filament centerline. For each of the 50 filament geometries, we minimize the total percentage error metric E as defined in Section II F with respect to the blob parameter δ and the Stokeslet spacing Δs. Tables I and II report the value of these optimal parameters. From the tables, we see that for those geometries where the error can be made small (<10%), the optimal blob size is typically between $\tilde{a}$ and $3\tilde{a}$, while the spacing is similar to the blob size. In this regime

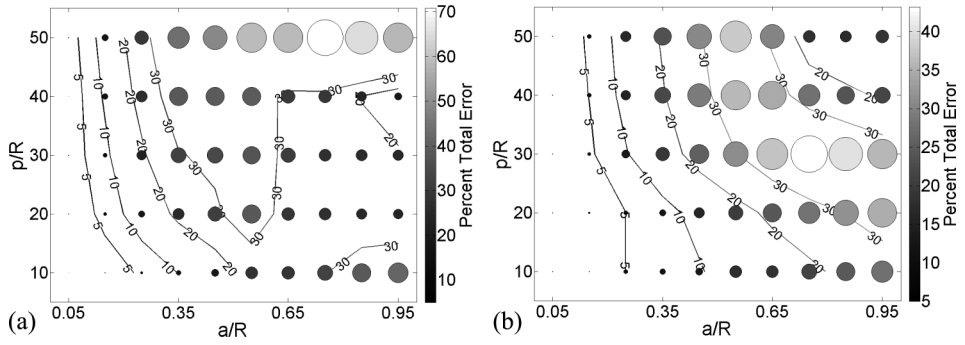

FIG. 4. Total error for (a) pump and (b) swimmer using centerline distribution of regularized Stokeslets. The size of circles at each investigated geometry is proportional to the total error (Eqs. (26) and (27)). Contour lines show interpolated errors.

of accuracy, both the optimal spacing and blob size tend to increase as $\tilde{p}$ increases. Our result for optimal blob size is consistent with the results of Bouzarth and Minion,[36] who found an optimal blob size of $1.43a$ for slender prolate ellipsoids with aspect ratios >10, which might be used to model straight rods.

Fig. 4 shows the total error for each geometry for pumping and swimming, respectively. In these figures, the circle size is scaled according to the percent error, and interpolated contour lines are drawn at 5, 10, 20, and 30 percent error in order to give a visual representation of the regions of accuracy. From the results, we make the following observations. First, the centerline distribution of regularized Stokeslets is more accurate for the swimmer than the pump. Second, this numerical method is most accurate for thin filaments (where $\tilde{a}$ is relatively small) and not accurate for the thickest filaments examined. For example, comparing to Fig. 1(b), this numerical method is quite accurate (with errors less than 5%) in the modeling of the flagella of bacteria such as *Salmonella* and *E. coli* as well as spermatozoa, but not accurate (with errors of approximately 25% in each scenario) for spirochetes such as *L. illini* and *B. burgdorferi*.

C. Slender body theory

We perform a similar investigation by comparing results for the slender body theory outlined in Section II to the benchmark results. In this numerical method, the total error is minimized with respect to the parameter q (recall that the length of the individual cylindrical segments is $2q$). Tables I and II report the optimal value of q for each geometry. From the tables, we see that accurate results are produced when both $q/\tilde{a} > 5$ (the segment length is at least 5 times the diameter) and $N \gtrsim 45$ ($\gtrsim$15 segments per turn). For slender body theory, we only report error values for the first 25 geometries since the error grows rapidly as a/R increases. This is consistent with expectations for this method: as the filament radius approaches the helical radius, the filament is less slender, and so it follows that a slender body theory approach would break down.

Fig. 5 shows the total error for each geometry for pumping and swimming, respectively. The total error in the slender body theory is within a tolerable range (<10%) only for $\tilde{a} \lesssim 0.10$. We note that the total error using the method of regularized Stokeslets on the filament centerline is also quite low for these particularly slender geometries, so in this range, we must make a judgement based on computational cost to compare the two methods.

D. Resistive force theory

Table III shows the results of RFT using the drag coefficients from the theories of Gray and Hancock[21] and Lighthill.[20] Throughout the whole range, neither gives accurate results; for the coefficients derived by Lighthill, the total percent error is minimal at $E_{\text{Total}} = 26\%$ and for the coefficients derived by Gray and Hancock, the total percent error is minimal at $E_{\text{Total}} = 33.6\%$, both for the geometry specified by $\tilde{a} = 0.05$ and $\tilde{p} = 50$.

Although the total error is large throughout the range tested, it is interesting to note that if one only considers the error in swimming speed (separately reported in Table III), the coefficients

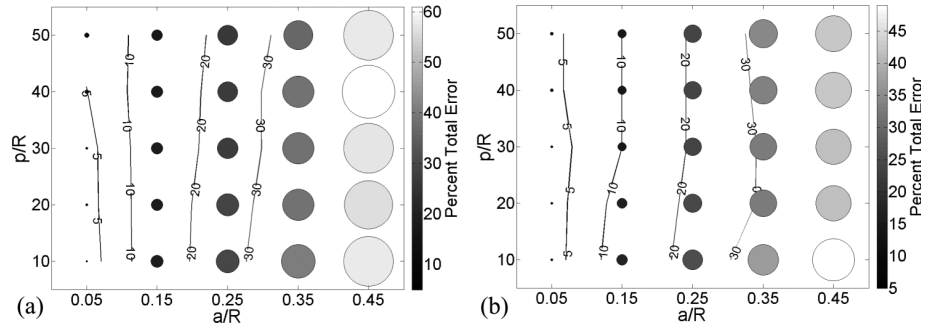

FIG. 5. Total error for (a) pump and (b) swimmer using slender body theory. The size of circles at each investigated geometry is proportional to the total error (Eqs. (26) and (27)). Contour lines show interpolated errors.

derived by Gray and Hancock produce accurate results for the swimming speed ($E_{\mathbf{V}} < 10\%$) for $\tilde{a} \leq 0.65$ and $\tilde{p} \geq 30$, a large range of geometries. In this regime, however, we find large errors in the filament torque. On the other hand, the theory of Lighthill produces accurate results for the filament torque for $\tilde{a} < 0.15$, but always gives large errors for the translational velocity. Thus, RFT may give accurate results for individual quantities, as has previously been observed in the literature, not only for swimming speeds but also for quantities such as distance traveled per revolution,[15] but does not accurately capture the full dynamics for any investigated geometry. Furthermore, without a more accurate benchmark comparison such as that performed here, it is difficult to know in advance if any particular quantity of interest will be accurately calculated using RFT.

IV. DISCUSSION

To summarize the results up to this point, based on a convergence study, we created benchmark results for swimming and pumping flows caused by helical filaments using a surface distribution of regularized Stokeslets. By comparison to the benchmark results, we found that resistive force theory does not give accurate results (in terms of total error) for any of the geometries studied. We also used the benchmark case to optimize the relevant parameters of a centerline distribution of regularized Stokeslets and slender body theory with respect to a total error metric and obtained regimes of accuracy for each numerical method. Together, Figs. 1, 4, and 5 allow us to make a judgement about which numerical method is appropriate for a wide variety of biological and artificial filament geometries. The regimes of accuracy for more cost efficient methods (SBT and centerline distributed regularized Stokeslets) overlap, so it is of interest to examine which numerical method will be optimal in terms of computational efficiency as well as total error. The computational cost of the numerical methods scales as N^3, where N is the number of collocation point. As noted before, a surface distribution of regularized Stokeslets (or any boundary element method) requires more and more collocation points as the filament becomes thinner since the spacing of the cross sections becomes smaller, but for slender filaments, SBT and centerline distributions of regularized Stokeslets are accurate and much cheaper computationally.

The overall choice for the cheapest numerical method which is still accurate can be summarized in Fig. 6. In this figure, we first choose an error threshold of 10% against the benchmarks obtained from the surface distribution of regularized Stokeslets. A contour is drawn for an interpolated 10% error threshold for each of the cheaper methods, which delineate three regions labeled near the bottom of each plot as "SBT" for the slender body theory, "CL" for the centerline distribution of regularized Stokeslets, and "SURFACE" for the surface distribution. These regions show the method which, given the 10% error threshold, is the most computationally efficient for a given geometry. Note that the regions are similar for the swimming and pumping scenarios, which suggests that these recommendations are broadly appropriate across many applications.

In order to provide information about the computational costs in each region, in Fig. 6, we also write the number of collocation points for each geometry tested. For the surface distribution region, we report the number of collocation points obtained by decreasing the number of collocation

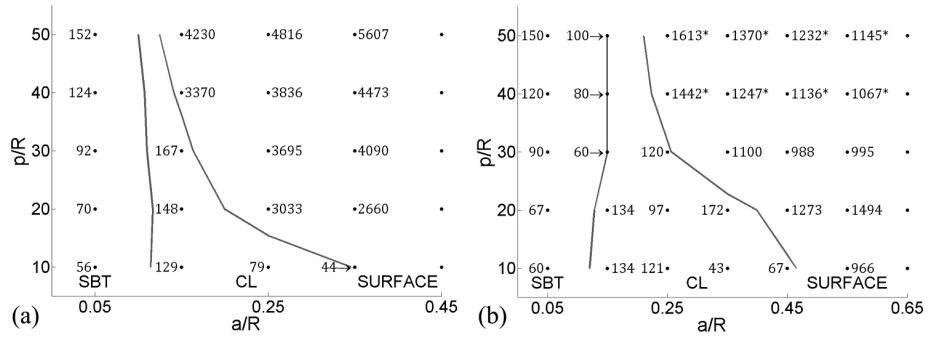

FIG. 6. Diagram of best choice of method (regions labeled above horizontal axis) to be used for 10% error in $\tilde{a}$-$\tilde{p}$ phase space for (a) pump and (b) swimmer based on computational efficiency. Note that the choice of method is broadly similar for both pumps and swimmers. Computational cost can be deduced from number at each geometry, which indicates optimal number of collocation points for the centerline distribution of regularized Stokeslets and slender body theory, and the number of collocation points needed to achieve 10% error for surface distribution of regularized Stokeslets.

points for each geometry by lowering the number of regularized Stokeslets per cross section n_c until we reach the error threshold of 10%. Points marked with an asterisk denote geometries for which the error of the surface distribution against the benchmark case was always less than 10%, even for the lowest number of regularized Stokeslets per cross section ($n_c = 3$). In these cases, the value of N using $n_c = 3$ is reported. This number allows us to compare to the costs required for the other methods. For the centerline distribution and SBT regions, we report the number of collocation points needed for the *optimal* accuracy parameters.

Within its regime of accuracy, we see that slender body theory requires approximately half as many collocation points as the centerline distribution of regularized Stokeslets. This means that the slender body theory may be up to ~10 times more computationally efficient in these regimes, which include more slender forms of bacterial flagella as well as spermatozoa. This result is consistent with the experimentally confirmed results of Rodenborn *et al.*[13] It should be noted that due to the addition of the dipole singularity (as well as the corresponding image system in the case of the pump), this method requires a larger initial investment for implementation than the method of regularized Stokeslets. Taking this into account, it becomes a value judgement in this regime as to whether the computational savings will be worth the initial effort in the long run.

For $0.15 < \tilde{a} < 0.40$, the centerline distribution of regularized Stokeslets provides a very efficient model for a wider range of physical examples. This range may include some bacterial flagella which are enveloped by a sheath, which makes them thicker than a bare flagellum, such as those of *H. pylori*[39] or *Vibrio* species.[40] Finally, as expected for the thickest filaments, such as the cell bodies of spirochetes or artificial helical microswimmers, the surface distribution of regularized Stokeslets is required for accurate results but increases the required number of collocation points by at least an order of magnitude.

In conclusion, the numerical methods tested — resistive force theory, slender body theory, and the method of regularized Stokeslets — have gained popularity due to their ease of implementation. We investigated their use throughout the range of geometries likely to be encountered in applications. In Tables I and II, we present optimized parameters for each method we study. Although in other geometries these precise parameters may not be optimal, they should provide useful starting points for tuning the parameters in other applications and geometries. For the case of a 10% accuracy threshold, Fig. 6 shows how an appropriate choice of method can be made for a wide range of filament geometries. Thus, our results provide necessary guidance for selection of computational method and should be useful for many future investigation involving filament induced flows.

ACKNOWLEDGMENTS

This work was supported by National Science Foundation Award Nos. DMR-1307497 and CBET-1252182.

APPENDIX: TABLES

TABLE I. Optimal parameters for centerline distribution and slender body theory, swimmer with head. For the slender body theory, only the first 25 entries are shown since error is large for all other (thick) geometries.

		Centerline				SBT		
$\tilde{a}$	$\tilde{p}$	$\Delta s/a$	δ/a	E_{swimmer} (%)	N	q/a	E_{swimmer} (%)	N
0.05	10	2.5	1.8	1.1	241	5	3	60
0.05	20	2.5	1.8	1.2	481	9	3	67
0.05	30	3.0	1.8	1.3	601	10	3	90
0.05	40	3.5	2.0	1.6	686	10	4	120
0.05	50	3.5	2.0	1.7	858	10	4	150
0.15	10	1.5	2.0	1.7	134	3	13	33
0.15	20	3.0	2.2	2.3	134	5	12	40
0.15	30	3.5	2.4	4.2	172	5	10	60
0.15	40	3.5	2.4	5.1	229	5	10	80
0.15	50	3.5	2.4	5.6	286	5	10	100
0.25	10	1.0	2.2	5.0	121	3	23	20
0.25	20	2.5	2.8	5.0	97	3	22	40
0.25	30	3.0	2.8	9.6	120	3	21	60
0.25	40	3.0	2.8	11.8	160	3	21	80
0.25	50	3.0	3.0	12.9	200	3	21	100
0.35	10	2.0	2.6	7.2	43	2	36	21
0.35	20	1.0	3.2	7.7	172	2	31	43
0.35	30	2.5	3.4	16.1	103	2	31	64
0.35	40	3.5	3.6	19.4	98	2	32	86
0.35	50	5.5	4.2	20.9	78	2	33	107
0.45	10	1.0	2.6	9.3	67	2	49	17
0.45	20	1.0	3.6	12.4	134	2	41	33
0.45	30	3.0	3.8	23.3	67	2	41	50
0.45	40	3.0	4.2	27.4	89	2	42	67
0.45	50	5.0	4.8	29.3	67	2	42	83
0.55	10	1.5	2.8	14.1	37			
0.55	20	1.0	3.8	17.0	110			
0.55	30	4.0	4.4	29.8	41			
0.55	40	3.0	4.4	35.3	73			
0.55	50	3.5	5.2	37.4	78			
0.65	10	1.5	3.0	14.9	31			
0.65	20	1.0	4.0	21.9	93			
0.65	30	4.5	4.6	36.7	31			
0.65	40	1.0	9.8	33.6	185			
0.65	50	1.0	10.0	28.5	231			
0.75	10	1.5	2.8	18.2	27			
0.75	20	1.0	4.0	26.1	81			
0.75	30	4.5	4.6	43.2	27			
0.75	40	1.0	9.4	25.8	161			
0.75	50	1.0	10.0	14.5	201			
0.85	10	2.0	3.0	22.3	18			
0.85	20	1.0	4.2	30.4	71			
0.85	30	1.0	7.8	40.1	106			
0.85	40	1.0	9.0	21.5	142			
0.85	50	1.0	9.6	13.5	177			
0.95	10	1.0	2.8	25.7	32			
0.95	20	1.0	4.2	34.0	64			
0.95	30	1.0	7.6	35.2	95			
0.95	40	1.0	8.6	19.1	127			
0.95	50	1.0	9.2	15.8	158			

TABLE II. Optimal parameters for centerline distribution and slender body theory, filament above no-slip surface. For the slender body theory, only the first 25 entries are shown since error is large for all other (thick) geometries.

		Centerline				SBT		
$\tilde{a}$	$\tilde{p}$	$\Delta s/a$	δ/a	E_{pump} (%)	N	q/a	E_{pump} (%)	N
0.05	10	0.91	2.01	0.95	562	5.3	2.6	56
0.05	20	1.01	2.27	1.66	1136	8.5	3.2	70
0.05	30	1.66	2.56	2.04	1063	9.7	3.3	92
0.05	40	1.36	2.74	1.46	1745	9.6	4.9	124
0.05	50	1.90	2.84	2.35	1568	9.9	6.1	152
0.15	10	1.33	2.27	2.79	129	3.1	14.2	32
0.15	20	2.60	2.75	6.35	148	4.8	14.0	41
0.15	30	3.54	3.22	8.67	167	5.1	14.1	58
0.15	40	4.37	3.74	10.85	182	5.3	13.8	75
0.15	50	5.28	4.24	12.58	189	5.3	12.7	94
0.25	10	1.31	2.57	5.64	79	3.0	27.0	19
0.25	20	3.10	3.46	13.72	75	3.2	26.3	37
0.25	30	4.10	4.42	18.69	87	3.2	24.1	56
0.25	40	4.20	5.37	23.02	114	3.3	23.8	72
0.25	50	3.61	6.25	26.47	166	3.3	23.2	90
0.35	10	1.70	2.76	10.20	44	1.9	38.9	22
0.35	20	1.95	4.10	21.86	85	2.0	36.6	42
0.35	30	2.19	5.60	29.44	116	2.0	36.4	64
0.35	40	2.37	7.28	36.29	144	2.0	36.8	85
0.35	50	2.56	8.82	41.82	168	2.0	34.3	107
0.45	10	1.78	2.89	14.43	33	1.8	58.0	18
0.45	20	0.46	4.86	28.57	278	1.8	56.1	37
0.45	30	0.73	8.05	31.93	270	1.8	57.4	55
0.45	40	0.90	9.36	36.83	294	1.9	61.0	70
0.45	50	0.85	9.65	47.54	391	1.9	57.8	87
0.55	10	1.34	2.93	24.23	36			
0.55	20	0.87	5.22	36.13	121			
0.55	30	1.04	8.54	35.09	156			
0.55	40	1.10	9.75	36.77	198			
0.55	50	1.10	10.05	58.54	248			
0.65	10	1.72	2.98	25.83	24			
0.65	20	0.45	5.16	25.91	197			
0.65	30	0.90	8.25	27.84	152			
0.65	40	0.96	9.35	27.22	192			
0.65	50	1.00	9.80	58.19	231			
0.75	10	1.81	3.01	29.52	20			
0.75	20	0.46	5.22	23.68	168			
0.75	30	0.92	7.96	23.77	129			
0.75	40	1.17	9.45	26.23	137			
0.75	50	1.47	10.54	70.87	138			
0.85	10	1.79	3.01	36.49	18			
0.85	20	0.46	5.05	21.13	148			
0.85	30	1.05	7.76	22.13	100			
0.85	40	1.18	9.18	19.71	120			
0.85	50	1.40	10.29	64.93	127			
0.95	10	1.51	2.95	39.67	19			
0.95	20	0.48	4.90	20.03	127			
0.95	30	1.12	7.63	21.04	84			
0.95	40	1.26	9.03	14.36	101			
0.95	50	1.35	10.00	57.54	118			

TABLE III. Resistive force theory results for swimmer computed using analytical resistance matrix for the ellipsoidal head. For the theories of Gray and Hancock, and Lighthill, we present the percent error in the translational velocity $\mathbf{V}$, filament torque $\mathbf{N_f}$, and the total percent error.

		Gray and Hancock			Lighthill		
$\tilde{a}$	$\tilde{p}$	$E_{\mathbf{V}}$ (%)	$E_{\mathbf{N_f}}$ (%)	E_{Total} (%)	$E_{\mathbf{V}}$ (%)	$E_{\mathbf{N_f}}$ (%)	E_{Total} (%)
0.05	10	26.95	35.95	44.9	69.80	5.54	70.0
0.05	20	16.77	36.32	40.0	51.90	5.82	52.2
0.05	30	9.89	34.88	36.3	41.58	6.14	42.0
0.05	40	7.45	34.17	35.0	32.21	6.80	32.9
0.05	50	6.03	33.09	33.6	25.11	6.56	26.0
0.15	10	28.18	47.39	55.1	70.94	10.19	71.7
0.15	20	15.40	46.23	48.7	54.92	12.89	56.4
0.15	30	7.40	44.75	45.4	42.42	14.04	44.7
0.15	40	7.18	43.60	44.2	32.16	14.56	35.3
0.15	50	8.05	42.55	43.3	24.69	14.67	28.7
0.25	10	31.00	56.10	64.1	69.80	16.92	71.8
0.25	20	15.04	54.58	56.6	57.35	21.94	61.4
0.25	30	6.12	53.11	53.5	44.18	23.49	50.0
0.25	40	6.46	52.09	52.5	33.50	24.35	41.4
0.25	50	8.18	51.26	51.9	25.87	24.85	35.9
0.35	10	31.04	62.86	70.1	65.59	23.45	69.7
0.35	20	14.74	61.52	63.3	59.44	30.64	66.9
0.35	30	6.00	60.51	60.8	46.15	33.09	56.8
0.35	40	6.95	59.63	60.0	35.44	34.17	49.2
0.35	50	8.53	58.96	59.6	27.93	34.89	44.7
0.45	10	34.97	68.73	77.1	61.24	30.46	68.4
0.45	20	15.70	67.46	69.3	62.46	38.85	73.6
0.45	30	5.93	66.48	66.7	49.07	41.34	64.2
0.45	40	7.62	65.84	66.3	38.21	42.75	57.3
0.45	50	9.10	65.30	65.9	30.94	43.60	53.5
0.55	10	36.49	73.24	81.8	53.97	36.04	64.9
0.55	20	16.47	72.16	74.0	64.75	45.65	79.2
0.55	30	7.25	71.36	71.7	52.40	48.41	71.3
0.55	40	8.06	70.78	71.2	41.70	49.83	65.0
0.55	50	8.45	70.26	70.8	34.73	50.62	61.4
0.65	10	39.06	76.92	86.3	45.78	40.77	61.3
0.65	20	18.03	75.97	78.1	67.66	51.40	85.0
0.65	30	9.20	75.27	75.8	55.89	54.26	77.9
0.65	40	9.00	74.68	75.2	45.79	55.57	72.0
0.65	50	9.54	74.19	74.8	39.39	56.32	68.7
0.75	10	40.88	79.85	89.7	35.97	44.49	57.2
0.75	20	19.99	78.98	81.5	70.74	56.04	90.2
0.75	30	11.38	78.33	79.1	60.19	58.92	84.2
0.75	40	11.16	77.77	78.6	50.74	60.19	78.7
0.75	50	11.71	77.27	78.2	44.78	60.85	75.6
0.85	10	41.96	82.21	92.3	27.42	47.31	54.7
0.85	20	22.69	81.44	84.5	74.45	59.90	95.6
0.85	30	14.18	80.79	82.0	64.97	62.72	90.3
0.85	40	13.96	80.23	81.4	56.20	63.90	85.1
0.85	50	14.98	79.69	81.1	51.11	64.45	82.3
0.95	10	44.65	84.18	95.3	33.16	49.55	59.6
0.95	20	25.65	83.45	87.3	78.24	63.11	100.5
0.95	30	17.62	82.79	84.6	70.29	65.84	96.3
0.95	40	17.83	82.21	84.1	62.33	66.93	91.5
0.95	50	19.53	81.64	83.9	58.13	67.35	89.0

[1] E. Lauga and T. R. Powers, "The hydrodynamics of swimming microorganisms," Rep. Prog. Phys. **72**, 096601 (2009).
[2] A. Ghosh and P. Fischer, "Controlled propulsion of artificial magnetic nanostructured propellers," Nano Lett. **9**, 2243–2245 (2009).
[3] A. Ghosh, D. Paria, H. J. Singh, P. L. Venugopalan, and A. Ghosh, "Dynamical configurations and bistability of helical nanostructures under external torque," Phys. Rev. E **86**, 031401 (2012).
[4] C. Peters, O. Ergeneman, B. J. Nelson, and C. Hierold, "Superparamagnetic swimming microrobots with adjusted magnetic anisotropy," in *2013 IEEE 26th International Conference on Micro Electro Mechanical Systems (MEMS)* (IEEE, 2013), pp. 564–567.
[5] K. E. Peyer, L. Zhang, B. E. Kratochvil, and B. J. Nelson, "Non-ideal swimming of artificial bacterial flagella near a surface," in *2010 IEEE International Conference on Robotics and Automation* (IEEE, 2010), pp. 96–101.
[6] S. Tottori *et al.*, "Assembly, disassembly, and anomoalous propulsion of microscopic helices," Nano Lett. **13**, 043705 (2013).
[7] Y. Ding, J. C. Nawroth, M. J. McFall-Ngai, and E. Kanso, "Mixing and transport by ciliary carpets: A numerical study," J. Fluid Mech. **743**, 124–140 (2014).
[8] H. Guo, J. Nawroth, Y. Ding, and E. Kanso, "Cilia beating patterns are not hydrodynamically optimal," Phys. Fluids **26**, 091901 (2014).
[9] M. J. Kim and K. S. Breuer, "Use of bacterial carpets to enhance mixing in microfluidic systems," J. Fluids Eng. **129**, 319–324 (2007).
[10] R. E. Johnson and C. J. Brokaw, "Flagellar hydrodynamics. A comparision between resistive-force theory and slender-body theory," Biophys. J. **25**, 113–127 (1979).
[11] N. Phan-Thien, T. Tran-Cong, and M. Ramia, "A boundary-element analysis of flagellar propulsion," J. Fluid Mech. **184**, 533–549 (1987).
[12] M. Ramia, D. L. Tullock, and N. Phan-Thien, "The role of hydrodynamic interaction in the locomotion of microorganisms," Biophys. J. **65**, 755–778 (1993).
[13] B. Rodenborn, C.-H. Chen, H. L. Swinney, B. Liu, and H. P. Zhang, "Propulsion of microorganisms by a helical flagellum," Proc. Natl. Acad. Sci. U. S. A. **110**, E338–E347 (2013), http://www.pnas.org/content/110/5/E338.full.pdf+html.
[14] Y. Hyon, Marcos, T. R. Powers, R. Stocker, and H. C. Fu, "The wiggling trajectories of bacteria," J. Fluid Mech. **705**, 58–76 (2012).
[15] H. C. Fu, M. Jabbarzadeh, and F. Meshkati, "Magnetization directions and geometries of helical microswimmers for linear velocity-frequency response," Phys. Rev. E **91**, 043011 (2015).
[16] N. Darnton and H. C. Berg, "Force-extension measurements on bacterial flagella: Triggering polymorphic transformations," Biophys. J. **92**, 2230 (2007).
[17] N. Darnton, L. Turner, S. Rojevsky, and H. C. Berg, "On torque and tumbling in swimming *Escherichia coli*," J. Bacteriol. **189**, 1756–1764 (2007).
[18] K. Hasegawa, I. Yamashita, and K. Namba, "Quasi- and nonequivalence in the structure of the bacterial flagellar filament," Biophys. J. **74**, 569–575 (1998).
[19] C. Brennen and H. Winet, "Fluid mechanics of propulsion by cilia and flagella," Annu. Rev. Fluid Mech. **9**, 339–398 (1977).
[20] J. Lighthill, "Flagellar hydrodynamics," SIAM Rev. **18**, 161–230 (1976).
[21] J. Gray and G. J. Hancock, "The propulsion of sea-urchin spermatozoa," J. Exp. Biol. **32**, 802–814 (1955).
[22] G. K. Batchelor, "Slender body theory for particles of arbitrary cross section in Stokes flow," J. Fluid Mech. **44**, 419 (1970).
[23] R. G. Cox, "The motion of long slender bodies in a viscous fluid. Part 1. General theory," J. Fluid Mech. **44**, 791–810 (1970).
[24] J. P. K. Tillett, "Axial and transverse Stokes flow past slender axisymmetric bodies," J. Fluid Mech. **44**, 401–417 (2001).
[25] J. R. Blake and A. T. Chwang, "Fundamental singularities of viscous flow. Part 1. Image systems in vicinity of a stationary no-slip boundary," J. Eng. Math. **8**, 23–29 (1974).
[26] R. Cortez and M. Nicholas, "Slender body theory for stokes flows with regularized stokeslets," Commun. Appl. Math. Comput. Sci. **7**, 33 (2012).
[27] J. L. L. Higdon, "A hydrodynamic analysis of flagellar propulsion," J. Fluid Mech. **90**, 685–711 (1979).
[28] S. Goldstein, K. Buttle, and N. Charon, "Structural analysis of the *Leptospiraceae* and *Borrelia burgdorferi* by high-voltage electron microscopy," J. Bacteriol. **178**, 6539–6545 (1996).
[29] A. Ghosh, P. Mandal, S. Karmakar, and A. Ghosh, "Analytical theory and stability analysis of an elongated nanoscale object under external torque," Phys. Chem. Chem. Phys. **15**, 10817–10823 (2013).
[30] C. Pozrikidis, *A Practical Guide to Boundary Element Methods with the Software Lirary BEMLIB* (Chapman and Hall/CRC, Boca Raton, FL, 2002).
[31] J. Ainley, S. Durkin, R. Embid, P. Boindala, and R. Cortez, "The method of images for regularized Stokeslets," J. Comput. Phys. **227**, 4600–4616 (2008).
[32] R. Cortez, "The method of regularized Stokeslets," SIAM J. Sci. Comput. **23**, 1204–1225 (2001).
[33] R. Cortez, L. Fauci, and A. Medovikov, "The method of regularized stokeslets in three dimensions: Analysis, validation, and application to helical swimming," Phys. Fluids **17**, 031504 (2005).
[34] S. Olson, S. Lim, and R. Cortez, "Modeling the dynamics of an elastic rod with intrinsic curvature and twist using a regularized stokes formulation," J. Comput. Phys. **238**, 169 (2013).
[35] S. D. Olson, S. S. Saurez, and L. J. Fauci, "Coupling biochemistry and hydrodynamics captures hyperactivated sperm motility in a simple flagellar model," J. Theor. Biol. **283**, 203–216 (2011).
[36] E. L. Bouzarth and M. L. Minion, "Modeling slender bodies with the method of regularized stokeslets," J. Comput. Phys. **230**, 3929–3947 (2011).
[37] S. Kim and S. J. Karrila, *Microhydrodynamics* (Dover, Mineola, New York, 2005).
[38] S. Childress, *Mechanics of Swimming and Flying* (Cambridge University Press, Cambridge, 1981).
[39] G. Geis, S. Sauerbaum, B. Forsthoff, H. Leying, and W. Opferkuch, "Ultrastructure and biochemical studies of the flagellar sheath of *Heliobacter pylori*," J. Med. Microbiol. **38**, 371–377 (1993).
[40] E. A. Follett and J. Gordon, "An electron microscope study of *Vibrio* flagella," J. Gen. Microbiol. **32**, 235–239 (1963).